Plasmonic Nanolaser Using Epitaxially Grown Silver Film

Yu-Jung Lu *et al.*

Science **337**, 450 (2012);
DOI: 10.1126/science.1223504

Plasmonic Nanolaser Using Epitaxially Grown Silver Film

Yu-Jung Lu,[1]* Jisun Kim,[2]* Hung-Ying Chen,[1] Chihhui Wu,[2] Nima Dabidian,[2] Charlotte E. Sanders,[2] Chun-Yuan Wang,[1] Ming-Yen Lu,[3] Bo-Hong Li,[4] Xianggang Qiu,[4] Wen-Hao Chang,[5] Lih-Juann Chen,[3] Gennady Shvets,[2] Chih-Kang Shih,[2]† Shangjr Gwo[1]†

A nanolaser is a key component for on-chip optical communications and computing systems. Here, we report on the low-threshold, continuous-wave operation of a subdiffraction nanolaser based on surface plasmon amplification by stimulated emission of radiation. The plasmonic nanocavity is formed between an atomically smooth epitaxial silver film and a single optically pumped nanorod consisting of an epitaxial gallium nitride shell and an indium gallium nitride core acting as gain medium. The atomic smoothness of the metallic film is crucial for reducing the modal volume and plasmonic losses. Bimodal lasing with similar pumping thresholds was experimentally observed, and polarization properties of the two modes were used to unambiguously identify them with theoretically predicted modes. The all-epitaxial approach opens a scalable platform for low-loss, active nanoplasmonics.

Miniaturization of semiconductor lasers holds the key to emerging applications in on-chip integration of nanophotonics and nanoelectronics (*1*–*3*). Currently, miniaturization of semiconductor lasers based on dielectric optical cavities is impeded by the diffraction limit—that is, $\sim(\lambda/2n)^3$ for three-dimensional (3D) cavities, where λ is the free-space wavelength and n is the refractive index of the dielectric (*4*–*7*). The recent advent of nanoplasmonics based on metallodielectric structures has led to the design of optical components and optoelectronic devices in the deep subwavelength regime (*8*–*13*). In particular, a new class of lasers based on surface plasmon amplification by stimulated emission of radiation (SPASER) has been proposed (*14*, *15*) and experimentally demonstrated (*16*–*19*). Surface plasmon polaritons (SPPs) excited in noble metal structures adjacent to gain media dramatically shrink the optical mode volume and provide the necessary feedback mechanism for a SPASER.

Among the available plasmonic cavity materials in the visible and near-infrared ranges, silver (Ag) is the best choice because of its minimal plasmonic damping (*20*). However, so far most plasmonic devices have their basis in granular polycrystalline Ag films, where surface roughness and grain boundaries lead to scattering of SPPs. Thus, atomically smooth or single-crystalline plasmonic structures are desirable building blocks for low-loss applications (*21*, *22*). With use of polycrystalline metallic materials, the lasing threshold for plasmonic nanolasers remains impractically high, and the continuous-wave (CW) operation of a plasmonic laser has yet to be demonstrated (*16*–*19*).

Having developed epitaxially grown, atomically smooth Ag films as a scalable plasmonic platform, we report a SPASER under CW operation with an ultralow lasing threshold at liquid nitrogen temperature and a mode volume well below the 3D diffraction limit. The device has its basis in the plasmonic nanocavity formed between epitaxial Ag film and a single nanorod consisting of a gallium nitride (GaN) shell and a green-emitting indium gallium nitride (InGaN) core, which acts as gain medium and which was chosen, in part, for its relatively large optical gain (*23*).

Under normal growth conditions, the nonwetting nature of low-loss noble metals on semiconductor or insulator substrates leads to granular film growth. The key to achieving smooth single-crystalline Ag film is to refine a two-step process (low-temperature deposition followed by room-temperature annealing) originally developed for GaAs(110) substrates (*24*, *25*) and to apply it to the silicon surface [Si(111), 7×7 reconstruction] (*26*). However, dewetting eventually occurs (*25*). This problem is solved by capping the as-grown Ag film with a thin dielectric layer.

During deposition at low temperature (90 K), Ag forms nanoclusters, as indicated by a spotty reflection high-energy electron diffraction (RHEED) pattern Fig. 1A, top). Upon annealing to room temperature, these nanoclusters smoothen, as indicated by streaky RHEED patterns (Fig. 1A, bottom). In situ scanning tunneling microscopy (STM) reveals that the surface is atomically smooth (Fig. 1B), with a surface step structure similar to that of the underlying Si(111) surface. The large-area film uniformity is confirmed by scanning tunneling spectroscopy (STS) (Fig. 1C), which reveals identical quantum well states at different locations on the sample surface (*24*, *25*). At the end of growth, the sample is capped with about 1.5 nm of amorphous germanium (Ge) grown by molecular beam epitaxy (MBE). Atomic force microscopy (AFM) reveals that the Ge-capped Ag film remains atomically smooth in air (Fig. 1D).

The nanocavity is defined by a GaN nanorod (480 nm in length) partially filled with an InGaN gain medium (170 nm in length) and separated

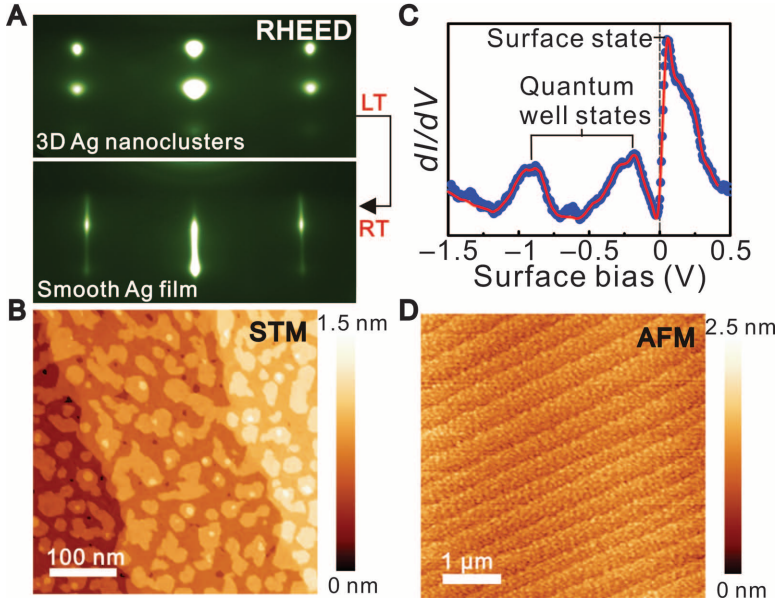

Fig. 1. (**A**) RHEED patterns taken during the two-step growth process. At low temperature (LT, 90 K), 3D Ag nanoclusters are observed after Ag deposition on Si(111). After room-temperature (RT) annealing, atomically smooth epitaxial Ag film forms. (**B**) In situ STM image of an atomically smooth epitaxial Ag film (4-nm thickness). (**C**) STS spectrum showing multiple quantum-well states and a surface state on epitaxial Ag film. Raw data (blue line) are shown with a superimposed smoothed spectrum (red line). (**D**) AFM image showing that Ge-capped Ag film remains atomically smooth in air (at RT).

[1]Department of Physics, National Tsing-Hua University, Hsinchu 30013, Taiwan. [2]Department of Physics, The University of Texas at Austin, Austin, Texas 78712, USA. [3]Department of Materials Science and Engineering, National Tsing-Hua University, Hsinchu 30013, Taiwan. [4]Beijing National Laboratory for Condensed Matter Physics and Institute of Physics, Chinese Academy of Sciences, Beijing 100190, China. [5]Department of Electrophysics, National Chiao-Tung University, Hsinchu 30010, Taiwan.

*These authors contributed equally to this work.
†To whom correspondence should be addressed. E-mail: shih@physics.utexas.edu (C.-K.S.); gwo@phys.nthu.edu.tw (S.G.)

by a 5-nm silicon dioxide (SiO_2) spacer from the epitaxial Ag (Fig. 2A). A nanoscale metal-oxide-semiconductor (MOS) structure is adopted here to confine the electromagnetic field in the low-dielectric-constant oxide nanogap, which greatly reduces plasmonic loss (*27*). The InGaN@GaN core-shell nanorods were grown on Si(111) by plasma-assisted MBE (*26*), with the nanorods growing along the wurtzite polar *c*-axis direction (*28*). Detailed structural information about the InGaN@GaN core-shell nanorods is given in Fig. 2, B and C.

Because the Ag layer is atomically flat and the core-shell nanorod has well-defined facets and contact geometry, a low-loss plasmonic cavity with atomically smooth interfaces is formed between them. Strong plasmonic confinement enables extraordinary localization of the hybrid optical mode around the nanorod, resulting in excellent spatial overlap between the mode and the gain medium and enabling the ultralow-threshold CW lasing operation in a diffraction-unlimited footprint. Figure 3A shows CW lasing spectra from a single nanorod at 78 K under varying optical power densities excited by a CW semiconductor diode laser at 405 nm. The scanning electron microscope (SEM) image in Fig. 2B depicts the actual core-shell nanorod on the epitaxial Ag film that was used for the reported lasing measurements. Two lasing peaks can be observed, at 510 and 522 nm. Investigations carried out with similar InGaN@GaN core-shell nanorods on a 20-nm polycrystalline Ag film (*26*) covered with a 5-nm SiO_2 spacer layer confirm that no lasing phenomena can be observed even at 8 K [under either continuous or pulsed pumping conditions; see figs. S6 and S7 (*26*)], which indicates the critical role of atomically smooth epitaxial Ag film for the observation of plasmonic lasing.

A light-light (*L-L*) plot shows the output power of the lasing mode at 510 nm as a function of pump power for two different temperatures, 8 and 78 K (Fig. 3B). The lasing signature can be seen from the concurrent onset of the linewidth narrowing plateau and the nonlinear kink of the "S"-shaped *L-L* plot. The lasing thresholds are 2.1 and 3.7 kW/cm^2 for the temperatures 8 and 78 K, respectively. For a single nanorod, these power densities correspond to threshold powers of 56 and 100 nW at the respective temperatures. In comparison with previously reported lasing thresholds for MOS-based plasmonic nanolasers under pulsed mode, our CW thresholds are at least two orders of magnitude smaller (*17*–*19*). Moreover, a high spontaneous-emission coupling factor β is estimated at 0.73, on the basis of fitting the *L-L* plot at 8 K; this indicates that the plasmonic cavity can effectively restrict undesired spontaneous emission in a single plasmonic mode under lasing conditions. The temperature-dependent emission properties, with lasing occurring for temperatures below 120 K (Fig. 3C), show that at higher temperatures only spontaneous emission occurs; this is because the reduced gain in InGaN cannot overcome the losses for the present device structure. The weak emissions at 532 and 556 nm, according to their *L-L* plots, are nonlasing peaks. The availability of multiple modes (510 and 522 nm) for such an ultrasmall cavity is due to the strong wavelength compression effects in plasmonic cavities. The second-order photon correlation function, $g^{(2)}(\tau)$, can provide another unambiguous signature for lasing in small cavities (*7*). As shown in Fig. 3D, below the lasing threshold $g^{(2)}(\tau = 0)$ is greater than one, signifying spontaneous emission. Above the lasing threshold, we confirm that $g^{(2)}(0) = 1$ and remains at unity for all τ, which is an unambiguous signature for the temporal coherence of lasing.

Three-dimensional simulations of the plasmonic nanolaser using COMSOL finite-element code (www.comsol.com) were carried out to clarify the nature of the two lasing modes, to determine their quality factors (*Q* factors) and lasing thresholds, and to elucidate the role of the atomically smooth Ag film in low-pumping-threshold lasing. The optical response of InGaN was described by an idealized single-resonance frequency-dependent permittivity function $\varepsilon_g = \varepsilon_\infty^g - \frac{\omega_P^2}{\omega_G^2 - \omega^2 - i2\omega\gamma_G}$. Here, ω_G is the emission peak; ε_∞^g is the high-frequency permittivity of the gain medium; $\gamma_G = \omega_G/2Q_{nr}$ is the nonradiative linewidth of the emitters, with Q_{nr} the emitters' nonradiative *Q* factor ($Q_{nr} \approx 17$); and ω_p is the effective plasma frequency of photoexcited carriers, as determined by the population inversion and proportional to the pumping power. The eigenvalue simulations reveal the existence of two dominant high-*Q* modes [labeled $Q^{(n)}$, where *n* is the integer number of charge density nodes inside the semiconductor rod] spectrally overlapping with the gain region responsible for lowest-threshold lasing. In the absence of optical pumping (i.e., for $\omega_p^2 = 0$), these $n = 5$ and $n = 4$ modes have the highest *Q* factors—$Q^{(5)} \approx 13$ and $Q^{(4)} \approx 9$—and Purcell factors—$F_P^{(5)} \approx 1.8$ and $F_P^{(4)} \approx 1.4$, respectively—as well as strongly subdiffraction mode volumes, $V \approx 0.03\lambda^3$ (*26*). The free-space emission profiles for the two modes are very different and can be easily identified. The $n = 5$ mode possesses a finite electric dipole moment d_x along the rod's length, responsible for highly *x*-polarized far-field emission, as shown in Fig. 4A (a schematic of the emission geometry is shown in Fig. 4C). On the contrary, $d_x = 0$ for the $n = 4$ mode, and the far-field radiation is dominated by the nonvanishing quadrupolar moments Q_{xx} and Q_{yy} (*29*) of the total charge distribution inside the hybrid plasmonic/photonic antenna. The emitted light's

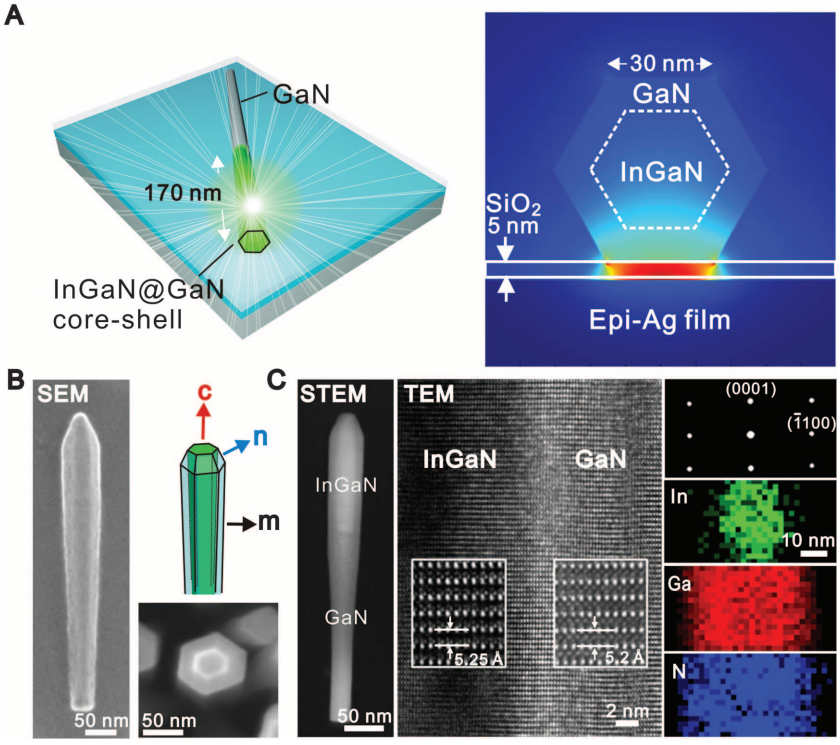

Fig. 2. (**A**) Schematic of device: a single InGaN@GaN core-shell nanorod on a SiO_2-covered epitaxial Ag film (28 nm thick). The energy-density distribution (right) is calculated by the eigenmode method. (**B**) SEM images of InGaN@GaN core-shell nanorods. The left-hand SEM image shows the actual nanorod on epitaxial Ag film that was used for all lasing measurements. (**C**) Scanning transmission electron microscopy (STEM) and transmission electron microscopy (TEM) structural analyses of a single-crystalline InGaN@GaN core-shell nanorod. The bright area inside the nanorod in the high-angle angular dark field STEM image indicates the presence of the InGaN core. The elemental mapping images obtained by energy dispersive x-ray spectroscopy are used to confirm the core-shell structure and to estimate the In composition in InGaN core (~14%).

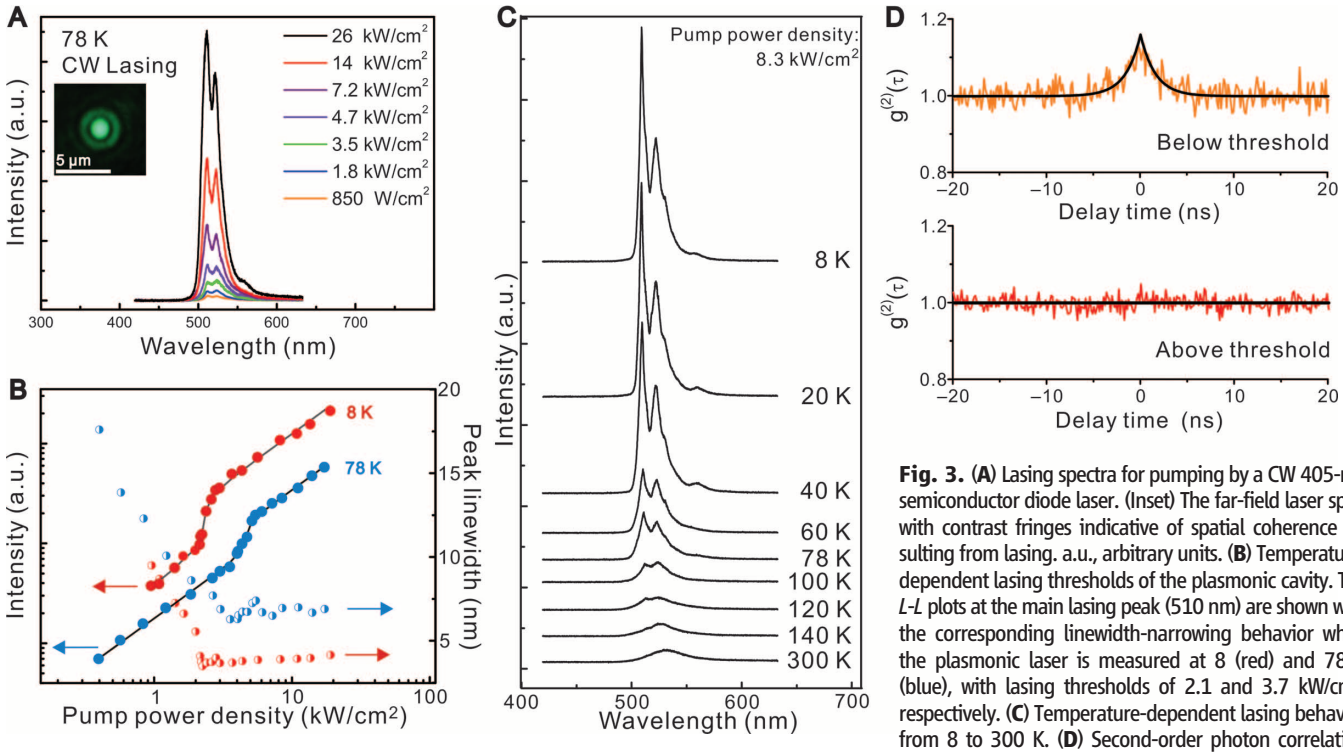

Fig. 3. (**A**) Lasing spectra for pumping by a CW 405-nm semiconductor diode laser. (Inset) The far-field laser spot, with contrast fringes indicative of spatial coherence resulting from lasing. a.u., arbitrary units. (**B**) Temperature-dependent lasing thresholds of the plasmonic cavity. The *L-L* plots at the main lasing peak (510 nm) are shown with the corresponding linewidth-narrowing behavior when the plasmonic laser is measured at 8 (red) and 78 K (blue), with lasing thresholds of 2.1 and 3.7 kW/cm^2, respectively. (**C**) Temperature-dependent lasing behavior from 8 to 300 K. (**D**) Second-order photon correlation function measurements at 8 K.

polarization is mixed between *x* and *y* (Fig. 4B). Indeed, as can be seen from Fig. 4D, the experimentally observed bimodal lasing modes (510 and 522 nm) are highly polarized along the rod axis, with a polarization ratio of 96% for the 510-nm mode and 60% for the 522-nm mode (simulation predicts 100% and 69% polarization, respectively, for a collection geometry with a numerical aperture = 0.55 objective).

Eigenvalue simulations (*26*) clarify the relative importance of the four physical processes determining the modes' lifetimes: ohmic loss in the metal, emission of SPPs to outside the cavity, radiation leakage into the substrate, and far-field emission. The most important lifetime-limiting factor is SPP emission to outside the cavity; this, for atomically smooth metal, occurs only at the ends of the GaN nanorod. Therefore, the nanolaser is a highly efficient source of coherent SPPs and can be classified as a SPASER (Fig. 4C). The prevalence of SPP generation also explains why atomically smooth metal is crucial for low-threshold CW lasing: Grain boundaries in polycrystalline Ag cause additional SPPs to be scattered out of the cavity. Our 3D simulations indicate a precipitous increase in modal volume for granular Ag (*26*), which explains the absence of CW lasing for polycrystalline Ag in the present experiment. Simulations also show that, because modes' intrinsic Q factors are comparable with the nonradiative Q factors of the emitters [$Q_{nr} \approx Q^{(n)}$], considerable hybridization between inhomogeneously broadened emitters and plasmonic modes takes place as ω_p^2 increases with pumping. Considerable blue-shifting (*26*) and rapid linewidth decrease of the emitter and nanocavity polaritons are the main experimentally observed signatures of such hybridization.

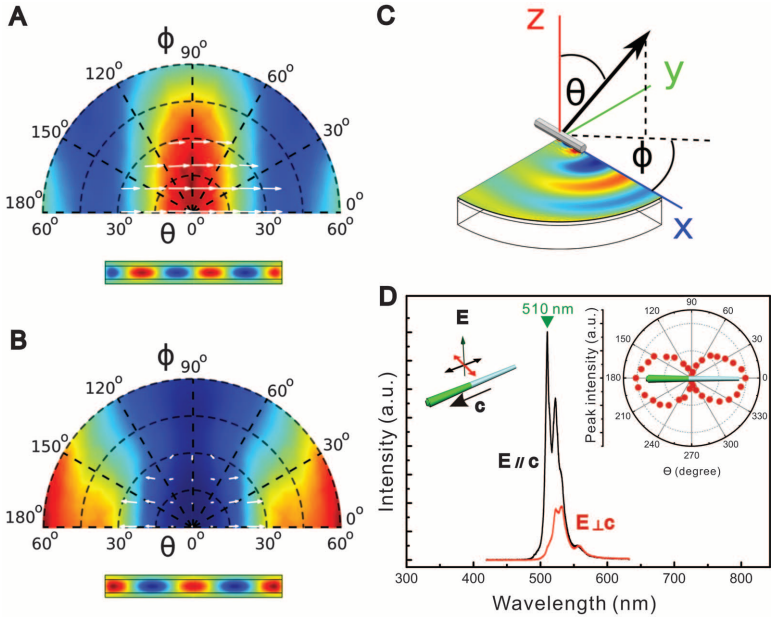

Fig. 4. (**A** and **B**) Simulations of the far-field radiation patterns (color-coded far-field radiation intensity) for two experimentally observed lasing modes. Surface charge distribution below the nanorod is color-coded. (**C**) Simulated emission geometry, showing that in-plane coherent SPPs are generated at the ends of the GaN nanorod. (**D**) Polarization-sensitive lasing spectra at 8 K, with the emission polarization oriented parallel (black curve) and perpendicular (red curve) to the nanorod axis (the *c* axis of wurtzite structure). (Inset) The polar plot of the emission intensity at 510 nm.

In summary, the development of atomically smooth epitaxial Ag on Si as a new platform for plasmonics not only allows us to demonstrate a SPASER-enabled nanolaser but also promotes the development of monolithically integrated plasmonics and Si-based electronics on a single platform.

References and Notes

1. S. Noda, *Science* **314**, 260 (2006).
2. H. Altug, D. Englund, J. Vučković, *Nat. Phys.* **2**, 484 (2006).
3. M. T. Hill, *J. Opt. Soc. Am. B* **27**, B36 (2010).
4. K. J. Vahala, *Nature* **424**, 839 (2003).
5. O. Painter *et al.*, *Science* **284**, 1819 (1999).
6. A. Tandaechanurat *et al.*, *Nat. Photonics* **5**, 91 (2011).
7. S. Strauf, F. Jahnke, *Laser Photon. Rev.* **5**, 607 (2011).
8. W. L. Barnes, A. Dereux, T. W. Ebbesen, *Nature* **424**, 824 (2003).
9. S. A. Maier, H. A. Atwater, *J. Appl. Phys.* **98**, 011101 (2005).
10. D. K. Gramotnev, S. I. Bozhevolnyi, *Nat. Photonics* **4**, 83 (2010).
11. J. A. Schuller *et al.*, *Nat. Mater.* **9**, 193 (2010).
12. M. T. Hill *et al.*, *Nat. Photonics* **1**, 589 (2007).
13. M. P. Nezhad *et al.*, *Nat. Photonics* **4**, 395 (2010).
14. D. J. Bergman, M. I. Stockman, *Phys. Rev. Lett.* **90**, 027402 (2003).
15. M. I. Stockman, *J. Opt.* **12**, 024004 (2010).
16. M. A. Noginov *et al.*, *Nature* **460**, 1110 (2009).
17. R. F. Oulton *et al.*, *Nature* **461**, 629 (2009).
18. R.-M. Ma, R. F. Oulton, V. J. Sorger, G. Bartal, X. Zhang, *Nat. Mater.* **10**, 110 (2011).
19. C.-Y. Wu *et al.*, *Nano Lett.* **11**, 4256 (2011).
20. P. R. West *et al.*, *Laser Photon. Rev.* **4**, 795 (2010).
21. P. Nagpal, N. C. Lindquist, S.-H. Oh, D. J. Norris, *Science* **325**, 594 (2009).
22. J.-S. Huang *et al.*, *Nat. Commun.* **1**, 150 (2010).
23. K. L. Shaklee, R. E. Nahory, R. F. Leheny, *J. Lumin.* **7**, 284 (1973).
24. A. R. Smith, K.-J. Chao, Q. Niu, C. K. Shih, *Science* **273**, 226 (1996).
25. H. Yu *et al.*, *Phys. Rev. Lett.* **88**, 016102 (2001).
26. Information on methods, analyses, and simulations can be found in the supplementary materials available on *Science* Online.
27. R. F. Oulton, V. J. Sorger, D. A. Genov, D. F. P. Pile, X. Zhang, *Nat. Photonics* **2**, 496 (2008).
28. Y.-J. Lu, H.-W. Lin, H.-Y. Chen, Y.-C. Yang, S. Gwo, *Appl. Phys. Lett.* **98**, 233101 (2011).
29. J. D. Jackson, *Classical Electrodynamics* (Wiley, New York, ed. 3, 1999), chap. 9.

Acknowledgments: We acknowledge support from the National Science Council in Taiwan (NSC-100-2120-M-007-001, NSC-98-2112-M-007-014-MY3, and NSC-98-2221-E-007-104-MY3) and, in the United States, the NSF (DMR-0906025, CMMI-0928664, and DGE-0549417), the Office of Naval Research (N00014-10-1-0929), the Air Force Office of Scientific Research (FA9550-08-1-0394), the Welch Foundation (F-1672), and the MOST of China (2009CB929102, 2012CB921302).

Supplementary Materials

www.sciencemag.org/cgi/content/full/337/6093/450/DC1
Materials and Methods
Supplementary Text
Figs. S1 to S7
References (*30*–*34*)

18 April 2012; accepted 14 June 2012
10.1126/science.1223504

Predictive Self-Assembly of Polyhedra into Complex Structures

Pablo F. Damasceno,[1]* Michael Engel,[2]* Sharon C. Glotzer[1,2,3]†

Predicting structure from the attributes of a material's building blocks remains a challenge and central goal for materials science. Isolating the role of building block shape for self-assembly provides insight into the ordering of molecules and the crystallization of colloids, nanoparticles, proteins, and viruses. We investigated 145 convex polyhedra whose assembly arises solely from their anisotropic shape. Our results demonstrate a remarkably high propensity for thermodynamic self-assembly and structural diversity. We show that from simple measures of particle shape and local order in the fluid, the assembly of a given shape into a liquid crystal, plastic crystal, or crystal can be predicted.

The spontaneous organization of individual building blocks into ordered structures is ubiquitous in nature and found at all length scales. Examples include simple and complex crystals in atomic systems, liquid and plastic crystals in molecular materials, and superlattices of nanoparticles and colloids. Understanding the relation between building blocks and their assemblies is essential for materials design because physical properties depend intimately on structure. The formation of atomic materials structures can be rationalized, to first approximation, from geometric considerations (*1*), and with growing length scale, the shape of the building blocks becomes increasingly important. For colloidal particles interacting through the excluded volume arising from their shape (*2*–*5*), thermodynamic equilibrium structures ("phases") reported were relatively simple (*6*–*10*). The simulation prediction of a dodecagonal quasicrystal with tetrahedra (*11*) demonstrated the unexpected complexity that could be achieved for particles solely with hard interactions. Since then, ordered structures have been reported for various polyhedra (*11*–*16*), which are now routinely synthesized as nanocrystals (*4*, *5*, *13*, *17*). However, the a priori prediction of structure from particle shape has yet to be demonstrated.

The thermodynamic behavior of hard particles can be understood through entropy maximization (*18*). Packing efficiency plays an increasingly important role toward higher density and induces a preferential alignment of flat facets (*13*, *19*, *20*). Because packing efficiency increases with contact area, the alignment can be interpreted as the result of an effective, many-body directional entropic force (*14*) arising from the increased number of configurations available to the entire system, causing suitably faceted polyhedra to order. This notion of directional entropic forces and their relation to particle faceting suggests that particle shape can be used to predict assembled structures. To establish clear quantitative trends, however, requires data on many different shapes. We present thermodynamic Monte Carlo simulations of the self-assembly of 145 different polyhedra, including all the Platonic, Archimedean, Catalan, and Johnson solids and some zonohedra, prisms, and antiprisms, and we show that we can use particle shape to predict the general category of ordered structure that forms.

The polyhedra simulated, classified according to the structure(s) they assemble into from the dense fluid, are shown in Fig. 1. The names of each polyhedron simulated and additional details can be found in fig. S1 and table S1 (*21*). We group polyhedra into three assembly categories (*12*): (i) crystals, (ii) plastic crystals, and (iii) liquid crystals. Polyhedra that are not observed to form ordered structures are grouped as (iv) disordered solids (glasses). The categories are further subdivided into classes based on the type of order and crystallographic symmetry. All structures reported form repeatedly from disordered fluid phases at packing fractions between 0.49 and 0.63, depending on particle shape. We first note that 101/145 ≈ 70% of the polyhedra simulated assemble on the time scale of our simulations, which demonstrates a strong propensity for order in systems of polyhedra, even in the absence of explicit attractive interactions.

For crystals, we find five different Bravais lattices [hexagonal, cubic, body-centered tetragonal (BCT), rhombohedral, and orthorhombic]. The lattice shear we find with truncated cubes has been observed in experiments (*13*, *22*, *23*). The A5 lattice, graphite structure, honeycomb lattice, diamond structure (*14*), and "supercube" lattice are periodic and have only a few particles in the unit cell. The quasicrystals have been reported previously with tetrahedra (*11*) and triangular bipyramids (*24*). A new type of hexagonal random tiling forming independent layers is observed for the bilunabirotunda, a two-dimensional version of the random tiling seen in a molecular network (*25*).

Both the diversity and structural complexity possible with polyhedra are demonstrated by 12 representative structures. Four examples of crystals are analyzed in more detail. Dürer's solids form a simple cubic crystal (Fig. 2A), which is unusual because it is a degenerate crystal (*26*). Particles align randomly in four equivalent orientations. The space-filling gyrobifastigium assembles into a crystal isostructural to β-Sn, the metallic form of tin (Fig. 2B). Six square pyramids assemble into cubes ("supercubes") and then into a slightly sheared simple cubic lattice (Fig. 2C). The supercubes demonstrate the possibility of hierarchical

[1]Applied Physics Program, University of Michigan, Ann Arbor, MI 48109, USA. [2]Department of Chemical Engineering, University of Michigan, Ann Arbor, MI 48109, USA. [3]Department of Materials Science and Engineering, University of Michigan, Ann Arbor, MI 48109, USA.

*These authors contributed equally to this work.
†To whom correspondence should be addressed. E-mail: sglotzer@umich.edu